Volume 1 | Number 1 | Jan 2013 | Pages 1–100

Catalysis
Science &
Technology

www.rsc.org/catalysis

ROYAL SOCIETY
OF CHEMISTRY

This is an *Accepted Manuscript*, which has been through the Royal Society of Chemistry peer review process and has been accepted for publication.

Accepted Manuscripts are published online shortly after acceptance, before technical editing, formatting and proof reading. Using this free service, authors can make their results available to the community, in citable form, before we publish the edited article. We will replace this *Accepted Manuscript* with the edited and formatted *Advance Article* as soon as it is available.

You can find more information about *Accepted Manuscripts* in the **Information for Authors**.

Please note that technical editing may introduce minor changes to the text and/or graphics, which may alter content. The journal's standard **Terms & Conditions** and the **Ethical guidelines** still apply. In no event shall the Royal Society of Chemistry be held responsible for any errors or omissions in this *Accepted Manuscript* or any consequences arising from the use of any information it contains.

ARTICLE

MeO$_x$/Al$_2$O$_3$ and MeO$_x$/CeO$_2$ (Me = Fe, Co, Ni) catalysts for high temperature N$_2$O decomposition and NH$_3$ oxidation

L. G. Pinaeva,*[a] I. P. Prosvirin,[a,b] L. S. Dovlitova,[a] I. G. Danilova,[a] E. M. Sadovskaya[a,b] and L. A. Isupova[a]

A series of MeO$_x$/Al$_2$O$_3$ and MeO$_x$/CeO$_2$ (Me = Fe, Co, Ni) was prepared by incipient wetness impregnation and characterized by XRD, XPS, UV-Vis DRS, differential dissolution phase analysis (DDPA). Their activity towards N$_2$O decomposition and ammonia oxidation at 750 – 900 ^{o}C was shown to depend on oxygen mobility in the sample as characterized by steady state isotopic transient kinetic analysis (^{18}O SSITKA) and dispersion of MeO$_x$ (Me = Fe) species. Obvious reverse "activity - FeOx dispersion" dependence was related to change of contribution from oxygen transfer from the support to active sites through Me-ceria or, it is not improbable, Me-alumina interface. It was shown that high efficiency of Fe/CeO$_2$ samples in deN$_2$O can be additionally increased after CeO$_2$ supporting onto high surface area alumina, ammonia oxidation to NO$_x$ being the same.

1. Introduction

Secondary abatement processes of N$_2$O formed as undesirable by-product at the catalytic oxidation of ammonia into nitric oxide implies catalyst set up in the ammonia burner operating at 800-900 ^{o}C directly after Pt-Rh gauzes [1]. Bulk or supported mixed metal oxides were developed for catalytic N$_2$O decomposition and put into practice in nitric acid plants before 2000 (Co$_2$AlO$_4$/CeO$_2$, CuO/Al$_2$O$_3$, La$_{0.8}$Ce$_{0.2}$CoO$_3$ and Fe/ZrO$_2$) [1]. Later, alternative catalytic formulations were evaluated as well, such as yttrium-doped zirconia [2], ceria-zirconia [3], A$_{1-x}$A$'_x$B$_{1-y}$B$'_y$O$_3$ perovskites with A = La or Ca, B = Mn, Co or Fe, A$'$ = Sr, B$'$ = Cu or Ni [4-6], metal-substituted hexaaluminates [7], Fe$_2$O$_3$-MeO$_x$ (Me= Al, Zr, Ce, La, Cu, Cr) obtained by co-precipitation [8, 9], Co$_3$O$_4$ [10] and CoO$_x$-CeO$_2$ [11] obtained by calcinations of mixtures of individual oxides. The pilot-plant reactor and real plant studies [8] confirmed high activity and very good mechanical stability of the Fe$_2$O$_3$/Al$_2$O$_3$ catalysts prepared by co-precipitation as well as no decomposition of nitric oxide. Several aspects with respect to the reaction mechanisms, the structure–activity correlations, the role of various gas inhibitors as well as the strategies followed to adjust the local surface structure of above mentioned noble metals free metal oxides were analyzed in the review of Konsolakis [12].

Ageing of Pt-Rh gauzes is accompanied by decrease of activity and yield of NO+NO$_2$ (NO$_x$), while N$_2$O production rises. With account of tendency of last decade to reduce platinum metal loading to the reactor (including number of gauzes and wire thickness), at gauzes deactivation noticeable slip of ammonia becomes possible followed by its reaction with NO$_x$. Therefore, development of bi-functional catalyst that is capable of efficient N$_2$O abatement and NH$_3$ oxidation to NO$_x$ becomes urgent for further optimization and reducing of harmful emissions of the process of HNO$_3$ production.

An idea of development of oxide-based catalyst that is capable to convert slipping ammonia with high selectivity to NO$_x$ was successfully realized by using dual bed system in which Fe$_2$O$_3$-Al$_2$O$_3$ based extruded monolith followed fewer number of platinum gauzes [13]. Later studies showed their efficiency of both slipping NH$_3$ oxidation to NO$_x$ and N$_2$O abatement [14]. At the same time, Al$_2$O$_3$ based honeycomb catalysts with the same geometry and FeO$_x$ based active component supported by impregnation were substantially more active in both reactions and retained high activity after the run in dual-bed system for 3 months [14].

Earlier we have shown that catalytic activity of Sr substituted La manganites in high-temperature N$_2$O decomposition correlated with the coefficient of lattice oxygen self-diffusion [5]. At using the materials with high bulk oxygen mobility the rates of oxygen transfer in the two-phase system "O$_{2gas}$–surface–catalyst bulk" characterized by ^{16}O/^{18}O exchange and N$_2$O decomposition additionally increased either at their decoration by structures characterized by higher rate of heteroexchange (composites LaSrFeO$_4$ (surface)–La$_{0.4}$Sr$_{0.6}$FeO$_3$ (bulk) [6]), or at modification of near surface layers by hetero cations (LaFeO$_3$-CeO$_2$ composites with Fe^{3+} ions inserted into fluorite lattice [15]). In the former case [6] "activity – oxygen mobility" correlation was observed for reaction of NH$_3$ oxidation as well. Pérez-Ramírez et al [16] showed that the reaction of NH$_3$ oxidation to NO$_x$ over oxide catalysts (Fe$_2$O$_3$, CeO$_2$, Cr$_2$O$_3$) follows a Mars–van Krevelen-type scheme with participation of lattice oxygen and reoxidation of the so-formed vacancies by both gas-phase O$_2$ and bulk lattice oxygen. Due to this, the efficiency of NH$_3$ oxidation to NO$_x$, especially in oxygen deficient conditions, depended on the rate of bulk oxygen diffusion to surface vacancies.

In accordance with these findings, the idea to combine high activity towards N_2O decomposition and NH_3 oxidation (at high selectivity to NO_x) in the same sample was checked. In addition to $Fe/Al_2O_3(CeO_2)$ samples, Co- and Ni- supported onto Al_2O_3 and CeO_2 were tried as well since a vast number of patent applications have claimed a relatively high NO selectivity (90–95%) using Co and Ni single metal oxides. Numerous attempts were done to commercialize Co_3O_4 based catalysts, but substantially lower activity and reversible deactivation of Co-systems, due to reduction of Co_3O_4 by NH_3 to the inactive CoO under reaction conditions in the upper parts of the bed excluded replacement of Pt gauzes by oxide catalysts. Nevertheless, these systems could be tried as the second catalyst in the dual bed system, especially provided stabilizing effect of CeO_2 in Co_3O_4-CeO_2 mixed oxides with low Co content is well-known [11]. Since copper catalyzes ammonium nitrate decomposition, an extremely important safety problem may arise if copper leaches from the catalyst and accumulates in the fertilizer product [1]. This undoubtedly completely excluded any Cu based system for using in the conditions of ammonia burner, although Cu/CeO_2 revealed high efficiency deN_2O at lower temperatures [17, 18] and more probably can be located after the absorption column. In addition, it is well known that under these conditions Cu-containing systems oxidize NH_3 to N_2 with high selectivity.

On the first stage we showed that intrinsic catalytic activity of different Me/Al_2O_3 (Me = Fe, Co, Ni) samples obtained by impregnation towards N_2O decomposition and NH_3 oxidation was substantially lower than for corresponding Me/CeO_2 samples with close surface Me concentration and correlated with the rate of oxygen exchange in the samples. Variation of Fe content in the $Fe/Al_2O_3(CeO_2)$ samples revealed noticeable reverse dependence of deN_2O and NH_3 oxidation activity due to size effect. In accordance with this, we supported FeO_x onto specially developed Al_2O_3 [19] characterized by high specific surface area, and formation of highly dispersed FeOx at increased Fe content in the sample finally resulted in N_2O and NH_3 conversion rise. For such samples we focused on Fe oxide as active component because in the case Me = Co, Ni low active $MeAl_2O_4$ or NiOx were formed on the surface of alumina. Using of the effect of high oxygen mobility in CeO_2 for this purpose was restricted by its low surface area at temperature of reaction, independently on preparation method [3, 20, 11]. Therefore, an attempt was done to disperse CeO_2 using precipitation onto high surface area Al_2O_3.

2. Experimental

2.1. Samples preparation

CeO_2 and Al_2O_3 samples used as the support was obtained by calcination of corresponding nitrate of chemical purity (99.5%) at 900 °C for 36 h. Al_2O_3 based supports were prepared by calcination of: 1) $Al(NO_3)_3*9H_2O$ of chemical purity (99.5%) at 1000 °C or 1200 °C for 6 h (denoted below as Al_2O_3-1000 and Al_2O_3-1200, respectively), or 2) product of centrifugal thermal activation of commercial-grade alumina hydrate (hydrargillite) [19] at 1000 °C for 19 h (Al_2O_3-C). To obtain Ce/Al_2O_3 support, the product of thermochemical activation of hydrargillite was first calcined at 500 °C (S_{BET} = 210 m²/g); then CeO_2 was precipitated onto this product from 0.75 M $Ce(NO_3)_3*6H_2O$ water solution using 1 M $(NH_4)_2CO_3$ as a precipitation agent, so that Ce : Al ratio in the final product was 1 : 1 (mole). The resultant precipitate was washed until the pH of the filtrate was 7, dried at 60 °C overnight, followed by calcination at 900 °C for 5 h.

All Me/support samples (Me=Fe, Co, Ni) were prepared by incipient wetness impregnation of corresponding support by water solution of Me nitrate with added citric acid in 10 wt.% excess to the stoichiometric amount to form the corresponding citrates and ethyleneglycole, dried in air at 150 °C for 3 h and then calcined at 900 °C for 4 h. In the commonly used abbreviation nMe/support "n" corresponded to Me weight content in the sample in terms of corresponding metal, although oxide compounds obviously formed. For CeO_2 and Al_2O_3-1200 the samples with Me concentration $6.7*10^{19}$ at/m² have been prepared which corresponded to Me content around 2.5-2.7 wt% (Al_2O_3-1200) and 0.86-0.91 wt% (CeO_2). For all supports we varied as well Fe content in the samples from 0.86 to 19.8 wt%. Bulk MeOx were obtained by calcination of chemical purity corresponding nitrates at 900 °C for 6 h.

2.2. Samples characterization

X-ray powder diffraction (XRD) patterns were recorded using Bruker D8 diffractometer with CuK_α monochromatic radiation. Each sample was scanned in the range of 2θ from 10° to 70° with a step 0.05° of 2θ. Surface composition of the samples was investigated by X-ray photoelectron spectroscopy (XPS) using spectrometer SPECS with Al K_α irradiation (hν = 1486.6 eV). Binding energy (BE) scale was preliminarily calibrated by the position of the peaks of Au $4f_{7/2}$ (84.0 eV) and Cu $2p_{3/2}$ (932.67 eV) core levels. UV-Vis diffuse reflectance spectra (UV-Vis DRS) were recorded using a UV-2501 PC Shimadzu spectrometer with an IRS-250A diffusion reflection attachment in the 11000-54000 cm⁻¹ range using the $BaSO_4$ as a reference. The edge energy (or band gap, Eg) for allowed transitions was determined by finding the intercept of the straight line for the low-energy rise of a plot of $[F(R_\infty) \, h\nu]^2$ versus $h\nu$ [21], where $h\nu$ is the incident photon energy, $F(R_\infty)$ is the Kubelka-Munk function.

The method of differential dissolution phase analysis (DDPA) was used to reveal the composition of the phases (including poorly crystallized, but without information about oxygen content therein) formed in the supported samples, including possible decoration of one phase by another [22]. For this about 10 mg of the sample was loaded in a microreactor and dissolved in the water based solvent with the composition changing from the lower towards higher acidity in the following order: 1) HCl (pH = 2), 2) (1÷3) M HCl, while the temperature increased continuously from 20 °C to 90 °C, 3) (3.6 M) HF and flowing the reactor with a flowrate at 3.6 ml/min. Change of the outlet mixture composition in time was analyzed by an atomic emission spectroscopy (BAIRD spectrometer) using following spectral lines of the elements (nm): Fe – 238.2, Al – 308.2, Ce – 413.8, Co – 238.8 with 5% accuracy of measurements at sensitivity level 10^{-3} µg/ml.

Kinetics of oxygen exchange was characterized by steady state isotopic transient kinetic analysis (SSITKA). For SSITKA experiments, sample (g = 0.025 g) loaded into a reactor (quartz tube, i.d. = 3 mm) was heated to 800 °C in 0.5% vol.$^{16}O_2$+He flow and kept at this temperature for 30 minutes, whereupon the gas mixture was replaced stepwise by the same one containing $^{18}O_2$ and Ar (1 vol.%) as an inert tracer. Gas flow rate for all mixtures amounted to 16.7 cm³/s. All responses were analyzed as time variation of the ^{18}O atomic fraction in the gas phase $\alpha_g(t)=(^{16}O^{18}O+2^{18}O_2)/(2\Sigma O^iO^j)$, where $\Sigma O^iO^j = {}^{16}O_2 + {}^{16}O^{18}O + {}^{18}O_2$ [23].

The catalytic activity for samples with particles of 250 – 500 µm in size was measured in a fixed-bed U-shaped reactor *(3 mm i.d. quartz tube)* at ambient pressure in the temperature range

750÷900 °C and contact time ~10^{-3}s. For NH_3 oxidation, mixture of 1%NH_3 in air or 1%NH_3 + 2%O_2 in N_2 was fed to the reactor charged by 0.015 or 0.043 g of the sample (see details in the text) with a flow rate 25 l/h. Outlet mixture composition was measured by IR spectroscopy. For N_2O decomposition, a gas mixture consisting of 0.15 vol% N_2O (+3%O_2+3%H_2O) in He flowed the reactor with a flow rate 60 l/h. For samples characterized by high specific surface area (Al_2O_3-C, Ce/Al_2O_3 based) we failed to reach reasonably low values of N_2O conversion at 800^0C. Therefore, the data obtained at the same sample loading (0.038 g) and flow rate (60 l/h) were considered to analyze the effect of Fe concentration. Outlet mixture composition was analyzed by on-line gas chromatograph with Porapack T (i.d. = 3mm, l = 3 m) and NaX (i.d. = 3mm, l = 2 m) columns.

3. Results and discussion

3.1. Phase composition
3.1.1. XRD analysis
Al_2O_3-1200 (Fig. 1a), Al_2O_3-1000 and CeO_2 used as the supports were single phase samples (Table 1), which values of coherent scattering area d_{XRD} calculated by the Scherrer equation were much less than the particle size estimated from the BET surface area (d_{BET}). For example, for Al_2O_3-1200 d_{XRD} = 360 Å, while d_{BET} = 3800 Å; for CeO_2-900 – 680 Å and 6400 Å, respectively. TEM images of CeO_2 sample revealed mixture of agglomerates composed of concreted crystallites of either 100 nm or 10 nm in a size [15]. The same can be reasonably supposed for Al_2O_3-1200 and Al_2O_3-1000 samples as well to explain the difference between d_{BET} and d_{XRD} values. Al_2O_3-C represented mixture of α- Al_2O_3 (Fig.1B, Table 1) with more dispersed θ-Al_2O_3, γ-Al_2O_3 and traces of κ-Al_2O_3. In the Ce/Al_2O_3 sample CeO_2 phase with the same lattice parameters but expected more dispersed, than in CeO_2 sample, species, θ-Al_2O_3 and traces of γ-Al_2O_3 were detected (Fig.1C, Table 1). Dispersion of θ-Al_2O_3

species was about the same as in Al_2O_3-C, as follows from close widening of peaks at 2θ~67° (γ-Al_2O_3 + θ-Al_2O_3), but cannot be calculated more precisely because of overlapping of its more intense peak at 2θ~32.9° with that of CeO_2.

Although Co_3O_4 and Co-Al-O spinels are characterized by the same symmetry group, increased lattice parameters of Co compounds in 2.7Co/Al_2O_3-1200 sample (Fig.1A) (a=b=c=8.104 (1) Å) compared with those in 0.91Co/CeO_2 one or bulk Co_3O_4 (a=b=c=8.084 (0) Å) favor formation of $CoAl_2O_4$ in the former [24], probably in the mixture with Co_3O_4. In the 2.7Ni/Al_2O_3-1200 and 2.5Fe/Al_2O_3-1200 samples, additional NiO with admixture of highly dispersed Ni-Al-O compounds of spinel structure and α-Fe_2O_3 were respectively detected. The lattice parameters of NiO and Fe_2O_3 in the supported samples were exactly the same as for bulk MeOx (not presented in the Table 1 for shortness). However, slight increase of α-Al_2O_3 lattice parameters in all Me/Al_2O_3 samples points to the probability of non-substantial Me^{n+} penetration into alumina lattice. With account of slightly higher radii of Me^{3+} ions compared with that of Al^{3+} (69÷74 pm and 67.5 pm, respectively), such assumption looks quite reasonable.

FeOx supporting onto Al_2O_3-C resulted in continuous decrease of the peaks corresponding to θ-, κ-, γ- Al_2O_3 with rise of Fe content from 2.5 to 13.2 wt% (Fig.1b). Instead of them second α-Al_2O_3 phase with increased lattice parameter (a=b=4.795 Å, c=13.057 Å) becomes evident and increases in the intensity (Table 1) that more obviously points to efficient incorporation of Fe^{3+} ions into the lattices of low temperature aluminas thus promoting their transition to α-Al_2O_3 at lower temperature [25]. This fact agrees well with decrease of S_{BET} value from 70 m^2/g for Al_2O_3-C to 22 m^2/g after supporting 19.8% of Fe (pattern of the last sample not presented for shortness).

In the patterns of (0.86-0.91)Me/CeO_2 samples traces of crystalline MeO_x were observed only for the case Me = Co, and some α-Fe_2O_3 was detected for substantially higher Fe content (sample 2.5Fe/CeO_2). Nevertheless, unlike to alumina based samples,
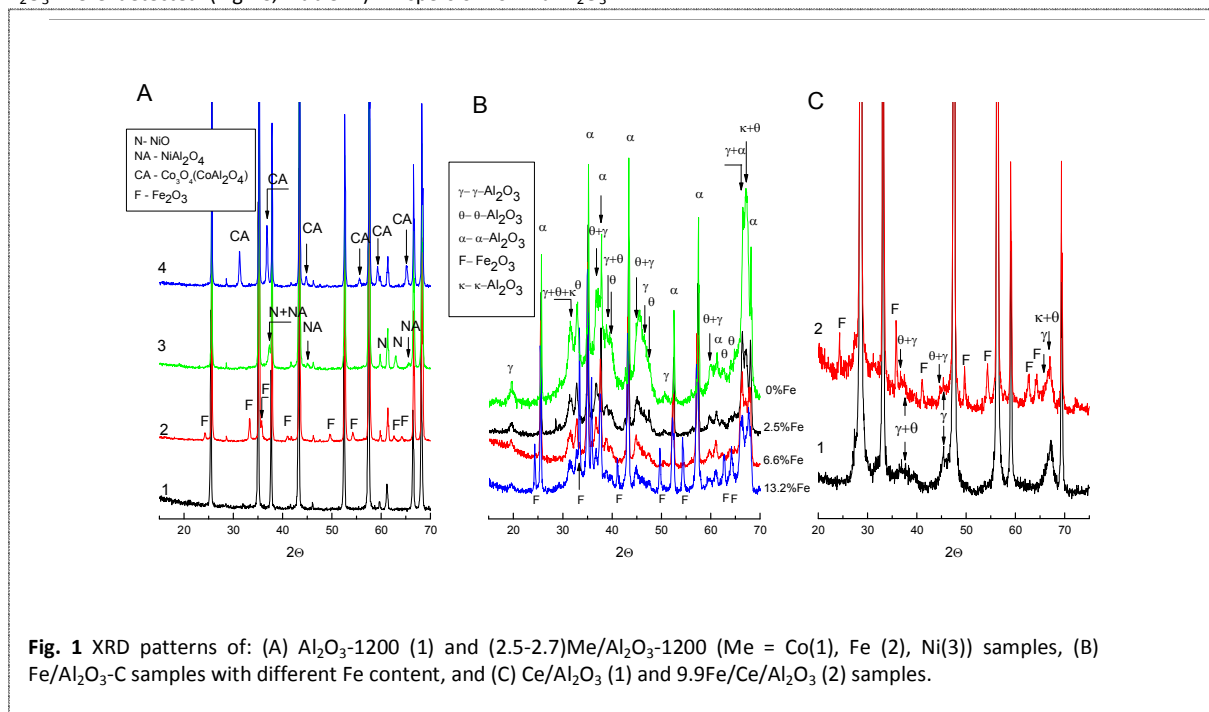

Fig. 1 XRD patterns of: (A) Al_2O_3-1200 (1) and (2.5-2.7)Me/Al_2O_3-1200 (Me = Co(1), Fe (2), Ni(3)) samples, (B) Fe/Al_2O_3-C samples with different Fe content, and (C) Ce/Al_2O_3 (1) and 9.9Fe/Ce/Al_2O_3 (2) samples.

Table 1 Phase composition, structural parameters, BET surface area and crystallite size estimated from XRD (d_{XRD}) of Al_2O_3, CeO_2 and MeO_x/CeO_2(Al_2O_3) samples.

Sample	S_{BET}, m²/g	Phase composition	d_{XRD}, Å
Al_2O_3-1200	4	α-Al_2O_3 (a=b=4.756 Å, c=12.986 Å)	370
Al_2O_3-1000	7	α-Al_2O_3 (a=b=4.760 Å, c=12.997 Å)	300
Al_2O_3-C	71	α-Al_2O_3 (a=b=4.771Å, c=13.020 Å)	480
		θ-Al_2O_3, κ-Al_2O_3, γ-Al_2O_3	100 (γ-Al_2O_3), 140 (θ-Al_2O_3)
2.5Fe/Al_2O_3-1200	4.0	α-Fe_2O_3 (a=b=5.035(0) Å, c=13.741 Å)	260
		α-Al_2O_3 (a=b=4.761 Å, c=12.997 Å)	500
2.7Co/Al_2O_3-1200	4.0	$CoAl_2O_4$ or Co_3O_4 (a=b=c=8.104 Å)	260
		α-Al_2O_3 (a=b=4.761 Å, c=12.997 Å)	520
2.7Ni/Al_2O_3-1200	4.0	NiO (a=b=c= 4.178 Å)	240
		$NiAl_2O_4$	≤120
		α-Al_2O_3 (a=b=4.760 Å, c=12.996 Å)	580
2.5Fe/Al_2O_3-C	60	α-Al_2O_3 (a=b=4.778 Å, c=13.039 Å)	510
		θ-Al_2O_3, κ-Al_2O_3, γ-Al_2O_3	highly dispersed
6.6Fe- Al_2O_3-C	46	α-Al_2O_3: 31% - a=b=4.770 Å, c = 13.030 Å	510
		69% - a=b=4.795 Å, c=13.057 Å	470
		θ-Al_2O_3, κ-Al_2O_3, γ-Al_2O_3	highly dispersed
13.2Fe- Al_2O_3-C	33	α-Al_2O_3: 18% - a=b=4.760 Å, c = 13.000 Å,	510
		82% - a=b=4.795 Å, c=13.057 Å,	520
		traces of θ-Al_2O_3, κ-Al_2O_3, γ-Al_2O_3	highly dispersed
		Fe_2O_3 (a=b=5.032 Å, c=13.702 Å)	250
CeO_2	1.4	CeO_2 (a=b=c=5.412 Å)	680
0.91Co/CeO_2	1.4	CeO_2 (a=b=c=5.412 Å)	630
		Co_3O_4 (a=b=c=8.084 Å)	460
0.86Fe/CeO_2	1.4	CeO_2 (a=b=c=5.411 Å)	550
0.91Ni/CeO_2	1.4	CeO_2 (a=b=c=5.411Å)	600
2.5Fe/CeO_2	1.4	CeO_2 (a=b=c=5.412 Å)	650
		traces α-Fe_2O_3	-
CeO_2/Al_2O_3	63	CeO_2 (a=b=c=5.411 Å)	400
		θ-Al_2O_3 and traces of γ-Al_2O_3	highly dispersed
9.9Fe/Ce/Al_2O_3	35	CeO_2 (a=b=c=5.411Å)	460
		θ-Al_2O_3 and traces of γ-Al_2O_3	highly dispersed
		α-Fe_2O_3 (a=b=5.035Å, c=13.741 Å)	320

neither following sintering of CeO_2, nor change of CeO_2 lattice parameters was noted after Me supporting (Table 1). By considering the radius of Fe^{3+} ions (0.049-0.078 pm, depending on coordination and spin state) is smaller than that of Ce^{4+} ions in the typical cubic fluorite lattice (0.097-0.101 nm), expected lattice shrinkage took place at substantial Fe content in the mixed Fe_x-Ce_{1-x} oxides [26]. However, at x<0.05 even slight unit cell expansion was observed and related by authors to partial Ce^{4+} reduction to larger (1.23 Å) ion Ce^{3+} [27] during calcination in Fe^{3+} presence. Therefore, penetration of supporting Me to the CeO_2 lattice cannot be excluded, especially with account of concreted nanocrystallites present in the initial support.

In the 9.9Fe/Ce/Al_2O_3 sample α-Fe_2O_3 was detected with lattice parameter and d_{XRD} value close to that in 13.2Fe/Al_2O_3-C and 2.5Fe/Al_2O_3-1200 samples. Although Fe supporting onto Ce/Al_2O_3 resulted in noticeable drop of the surface area, like in Al_2O_3-C based samples, it didn't facilitate formation of α-Al_2O_3 (Tables 1-2, Fig.1C). For similar CeO_2/Al_2O_3 samples it was shown that this is Ce in the lower oxidation state that stabilizes alumina toward the formation of low-surface-area phases up to 1100 °C or 1200 °C K under oxidizing and reducing conditions, respectively [28]. Since $CeAlO_3$ crystallites at high temperature and under reducing conditions were

observed by XRD, stabilization of Ce^{3+} is more probably due to interaction with OH groups of alumina. Absence of such alumina-bonded hydroxyl groups can prevent penetration of Fe^{3+} into the bulk of alumina and phase transition observed in the case of Al_2O_3-C sample.

3.1.2. DDPA.

DDPA of (2.5-2.7)Me/Al_2O_3-1200 and (0.86-0.91)Me/CeO_2 samples has been performed to reveal: 1) possible modification of support lattice due to Me insertion, and 2) formation of Co-Al spinels. Al_2O_3-1200 supported samples were quite stable towards dissolution. So, about 5 wt% and 2 wt% of the 2.5Fe/Al_2O_3-1200 and 2.7Co/Al_2O_3-1200 samples respectively dissolved during all steps (Table 2). Nevertheless, all Fe supported onto Al_2O_3-1200 passed into the solution (Fig.2A): as individual oxide/hydroxide (about 18.4 mole% of the probe dissolved in HCl), while the rest Fe (~43.5 mole% of the probe) - in HF together with some Al. Since some dissolution of the last proceeded even after all Fe was removed from the sample, formation of Fe-Al solid solution is excluded, and the structure with FeOx species located on the surface or on the intergrain boundaries of concreted alumina micro-crystallites and linked to the last, more probably, due to penetration of some Fe^{3+} ions to the disordered

Table 2 Chemical composition of dissoluble part of Me/Al$_2$O$_3$-1200(CeO$_2$) samples (Me = Co, Fe, Ni).

Sample	Sample dissolved, weight%	Me, weight% of the sample in dissolved portion	Element	Distribution of elements dissolved during different steps but O, mole %			
				total	HCl (pH=2)	(1÷3)M HCl	(3.6)M HF
2.5Fe/Al$_2$O$_3$-1200	5	2.53	Al	38.1	-	-	38.1
			Fe	61.9	-	18.4	43.5
2.7Co/Al$_2$O$_3$-1200	2	0.43	Al	82.1	-	-	82.1
			Co	17.9	0.4	-	17.5
CeO$_2$	4	-	Ce	100	-	-	100
0.91Co/CeO$_2$	95	0.93	Ce	98.2	-	98.2	-
			Co	1.8	traces	0.39	1.41
0.86Fe/CeO$_2$	54	1.0	Ce	96.8	-	96.8	-
			Fe	3.2	0.60	1.86	0.74
0.91Ni/CeO$_2$	11	0.81	Ce	91.3	-	-	91.3
			Ni	8.7	traces	7.8	0.9

near subsurface layers can be considered. In the case of 2.7Co/Al$_2$O$_3$-1200 only 0.43 wt% of Co dissolved in all steps, and overwhelming majority – as the solid solution with Co$_{0.3}$Al$_1$ stoichiometry reasonably related to the mixed Co-Al-O spinel like compounds located in the near surface layer of the sample. The nature of insoluble Co compounds still remained open.

CeO$_2$ didn't dissolve in HCl, and very slow dissolution (about 4% of the total sample weight for 7 minutes) took place after HF feeding (Fig.2B, Table 2). Me/CeO$_2$ samples dissolved in substantially milder conditions, but the character and the rate of their dissolution depended on Me nature. So, already 95 weight% of 0.91Co/CeO$_2$ sample dissolved in these conditions. Increase of solubility can be related first of all to formation of Co-Ce-O solid solution with Co/Ce = 0.004 and including all soluble Ce (dissolved in (1÷3) M HCl). This obviously means that Co^{3+} ions are capable to insert into more dispersed (~10 nm) concreted microcrystallites, and modify the lattice of larger (~100 nm) particles increasing their solubility. The rest of Co dissolved slowly as an oxide in the most rigid conditions (3÷6M HF), and, more probably, can be related to well-crystallized Co$_3$O$_4$ detected by XRD (Table 1). Absence of any Co in the same flow during dissolution of 2.7Co/Al$_2$O$_3$-1200 sample points to the formation of well-crystallized Co-Al spinel therein. Quantity of dissolved 0.86Fe/CeO$_2$ sample was some lower (54 wt% of the total) and, like in 2.5Fe/Al$_2$O$_3$-1200 case, all Fe passed into the solution (Fig.S1). It was included in Fe oxide/hydroxide which solubility in HCl (pH=2) and at the substantially higher acidity (3.6 M HF) can be due to different degree of crystallinity or defect structures formed. The parallel dissolution of remaining Fe and Ce in the flow of (1÷3)M HCl with the stoichiometry Fe/Ce = 0.02 points to formation of Fe-Ce-O solid solution, more probably, with participation of CeO$_2$ composites characterized by smaller sizes of crystallites. Unmodified ceria is stable even in 3.6 M HF and can be related to composites with largest crystallites. We cannot exclude that both unmodified CeO$_2$ and Ce-Fe-O solid solution are decorated by highly defective Fe oxide/hydroxide species dissolved in the weak HCl. In the case of 0.91Ni/CeO$_2$ sample (Fig. S1) most of supported Ni dissolved individually in (1÷3) M HCl, while the parallel Ni and Ce dissolution took place in the more rigid conditions (3÷6 M HF) and included only 10 weight% of the sample. Therefore, in the 2.7Co/Al$_2$O$_3$-1200 sample Al^{3+} ions partially replace Co^{3+} in the spinel structure, forming both highly disordered and well-crystallized Co-Al-O species, while incorporation of Fe^{3+} ions into the boundaries of the micro-composites results in the anchoring of Fe$_2$O$_3$ crystallites to alumina surface. Me-ceria interaction results in formation of Me-Ce-O solid solutions in
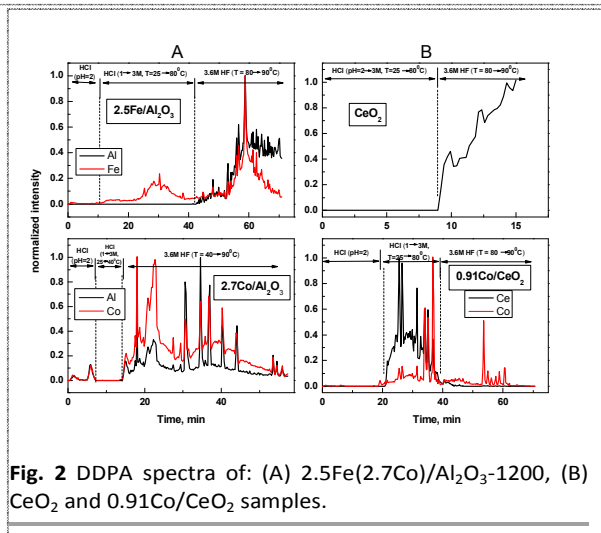

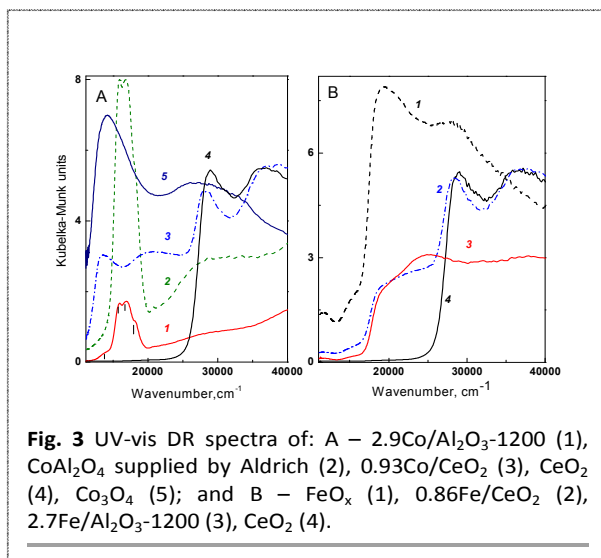**Fig. 2** DDPA spectra of: (A) 2.5Fe(2.7Co)/Al$_2$O$_3$-1200, (B) CeO$_2$ and 0.91Co/CeO$_2$ samples.

Fig. 3 UV-vis DR spectra of: A – 2.9Co/Al$_2$O$_3$-1200 (1), CoAl$_2$O$_4$ supplied by Aldrich (2), 0.93Co/CeO$_2$ (3), CeO$_2$ (4), Co$_3$O$_4$ (5); and B – FeO$_x$ (1), 0.86Fe/CeO$_2$ (2), 2.7Fe/Al$_2$O$_3$-1200 (3), CeO$_2$ (4).

Me/CeO$_2$ samples, their content and degree of disorder in the sample change in the following order: 0.91Co/CeO$_2$ > 0.86Fe/CeO$_2$ > 0.91Ni/CeO$_2$ ≥ CeO$_2$.

3.2. Microstructure

UV-Vis DR spectra of different Co- and Fe- based catalysts have been presented in the Fig.3a and Fig.3b, respectively. CeO_2 was characterized by strong a.b. at 36500 and 29000 cm^{-1} attributed to $Ce^{4+} \leftarrow O^{2-}$ charge transfer and the interband transitions, correspondingly [29], and band gap energy (E_g) value at 3.35 eV which is consistent with the reported value 3.3 eV [29-31]. The spectra of 0.91Co/CeO_2 (Fig.3a) and 0.86Fe/CeO_2 (Fig.3b) samples are in fact a superposition of those for corresponding bulk oxides and CeO_2, excluding the red shift of absorption edge of CeO_2 (E_g value at 3.18 and 3.22 eV for 0.91Co/CeO_2 and 0.86Fe/CeO_2, respectively) and additional absorption band at ~20000 cm^{-1} (Co case) and 23500 cm^{-1} (Fe case). Minimal value of red shift of absorption edge compared to that in the support was evaluated for 0.91Ni/CeO_2 sample (E_g value at 3.27 eV, spectrum not shown for brevity). Earlier we already observed these spectral characteristics for Fe/CeO_2 sample prepared by the same way [15] and explained their appearance by O_2 adsorption on the structural defect, more obviously, clusters of oxygen vacancies arose after entrance of dopant ions into the bulk of CeO_2. Like proposed in [30], change of the value of absorption edge indicate that either (1) Me ions in Me/CeO_2 samples substitute into the CeO_2 lattice; or (2) the isolated Me ions form mixed Me-Ce oxide and strongly interact with CeO2 leading to the electronic structure changes. In our case the value of the red shift correlated well with content of Me-Ce mixed solution in the sample, as determined by DDPA.

In the spectrum of 2.9Co/Al_2O_3-1200 sample an intense triplet of bands at about 15900, 17000 and 18200 cm^{-1} with the shoulder at 13800 cm^{-1} were detected and related to the transitions of $^4A_2 \rightarrow ^4T_1(^4P)$ of the tetrahedral Co^{2+} ions in Co-Al-O spinel and cobalt oxide, respectively [32]. Presence of the same triplet in the reference CoAl$_2$O$_4$ sample (Aldrich) evidences formation of Co-Al-O spinel with admixture of Co_3O_4.

3.3. Surface composition.

As follows from X-Ray photoelectron spectra of Ni 2p, Fe 2p, and Co 2p levels in Me/Al_2O_3-1200 and Me/CeO_2 samples presented in the Fig. 4, the nature of Me surface compounds depended on the support nature. Usually, no difference between various Co compounds can be reliably withdrawn from binding energies of either Co $2p_{1/2}$ or Co $2p_{3/2}$ signals [10] without accounting for the position of their satellites arising due to the shake-up process of Co^{2+} compound in the high spin state. Indeed, BE values characterizing Co $2p_{3/2}$ peak position in CoO, CoOOH and Co_3O_4 are indistinguishable (~780.0 eV). Higher but also very close BE values have been reported for CoAl$_2$O$_4$ and Co(OH)$_2$ (781.9 and 781.2 eV, respectively) [33-38]. However, for CoO, Co(OH)$_2$ or CoAl$_2$O$_4$ the satellite - main signal distances fall in the range 5-6.5 eV [34, 35, 39, 40], while the satellites in the spectrum of pure Co_3O_4 and CoOOH should be located approximately 9–10 eV away from the main signals [34,36,39]. In this regard, BE value of Co $2p_{3/2}$ signal at 781.6 eV with satellite at 786.6 eV in 2.7Co/Al_2O_3-1200 sample (Fig.4a) excluded CoO, Co_3O_4 and CoOOH from our consideration, and either Co(OH)$_2$ [33] or CoAl$_2$O$_4$ [34,37,38] could form on the surface. According to DDPA data, Co(OH)$_2$ could be responsible for about 0.4% of Co compounds (Table 2, corresponds to Co dissolved
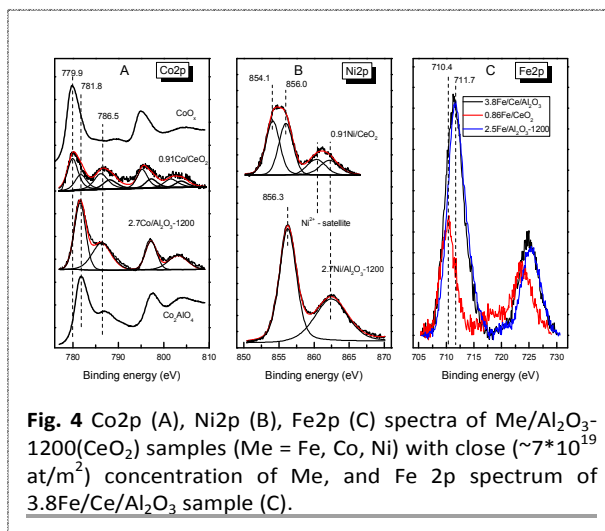

Fig. 4 Co2p (A), Ni2p (B), Fe2p (C) spectra of Me/Al_2O_3-1200(CeO_2) samples (Me = Fe, Co, Ni) with close (~7*10^{19} at/m^2) concentration of Me, and Fe 2p spectrum of 3.8Fe/Ce/Al_2O_3 sample (C).

in HCl at pH=2), therefore, most of surface Co included in the Co-Al spinel structures. To ensure the correctness of such assignment, spectrum of CoAl$_2$O$_4$ supplied by Aldrich and additionally calcined at 900 $^\circ$C for 5 h has been presented as well. In 0.91Co/CeO_2 sample the position of the main Co $2p_{3/2}$ peak shifted to lower BE values (779.9 eV), while the shoulder at 781.9 eV still was present resulting in the ratio of their intensities as ~3:2. Definite assignment of the peak at 779.9 eV to individual CoO, Co_3O_4 or CoOOH was impossible since presence of satellites at 786.7 and 790.8 eV agrees with formation of any of these compounds. In addition, in the XPS spectrum of bulk Co_3O_4 sample characterized by the same lattice parameters as for 0.91Co/CeO_2 sample (Table 1) intensity of satellite peak was substantially lower. Hence, different oxide/hydroxide-like Co compounds, including those in Co-Ce-O solid solution, have been formed on the surface of 0.91Co/CeO_2 sample. In particular, Co(OH)$_2$ in this case could result from hydration of highly dispersed species.

Ni $2p_{3/2}$ peak at 856.3 eV in 2.7Ni/Al_2O_3-1200 sample (Fig. 4b) can be due to both NiAl$_2$O$_4$ (BE ranging from 855.2 to 857.2 eV) and Ni(OH)$_2$ (855.6 - 856.6 eV) [41-45], the former being detected as well by XRD (Fig. 1, Table 1). NiO state characterized by lower BE value (854.2 eV) [45] was detected in the 0.91Ni/CeO_2 sample together with Ni(OH)$_2$ (NiO : Ni(OH)$_2$) $\approx$ 50 : 50) resulting in the widening of both main Ni 2p peak and energy shake up satellite peak about 6 eV above the main line. Like for 0.91Co/CeO_2 sample, Ni(OH)$_2$ detection could evidence presence of highly dispersed NiO species both in Al_2O_3 and for CeO_2 based samples. In this case, their relative content in the samples is higher compared with Co case.

While the BE value of the Fe $2p_{3/2}$ spectra in 0.86Fe/CeO_2 sample at 710.4 eV (Fig. 4c) evidences preferential Fe^{3+} state in the oxide, its high energy shift (BE = 711.8 eV) detected in both 2.5Fe/Al_2O_3-1200 specimen and all Al_2O_3-1000, Al_2O_3-1200 and Al_2O_3-C supported samples can be related to formation of mainly Fe^{3+} oxyhydroxide therein [46]. In the 3.8Fe/Ce/Al_2O_3 sample both states of Fe^{3+} have been detected as well, but fraction of Fe^{3+} state in the oxide is some higher than in Fe/Al_2O_3 based samples. Therefore, FeOx species anchor both to Al_2O_3 and CeO_2 surface.

Table 3 Physicochemical properties of different Me/Al$_2$O$_3$, Me/CeO$_2$ and 3.8Fe/Ce/Al$_2$O$_3$ samples.

Sample	S$_{BET}$, m^2/g	Me$_s$, at.% (by XPS)	Fe$_{exp}$, rel. units	D$_{Me}$, rel. units
CeO$_2$ based				
0.86Fe/CeO$_2$	1.3	1.0	1.3	1.5
0.91Co/CeO$_2$	1.3	1.2	-	1.8
0.91Ni/CeO$_2$	1.3	2.0	-	2.7
2.5Fe/CeO$_2$	1.3	1.5	2.1	0.72
Al$_2$O$_3$-1200 and Al$_2$O$_3$-1000 based				
2.5Fe/Al$_2$O$_3$-1200	4	1.1	4.4	1.6
2.7Co/Al$_2$O$_3$-1200	4	1.0	-	1.5
2.7Ni/Al$_2$O$_3$-1200	4	1.4	-	2.1
0.86Fe/Al$_2$O$_3$-1200	4	1.1	4.4	4.8
2.5Fe/Al$_2$O$_3$-1000	7	1.4	9.8	3.7
Al$_2$O$_3$-C based				
2.5Fe/Al$_2$O$_3$-C	61	0.46	28.1	10.5
6.6Fe/Al$_2$O$_3$-C	46	1.3	59.8	8.5
13.2Fe/Al$_2$O$_3$-C	33	2.2	72.6	5.1
19.8Fe/Al$_2$O$_3$-C	22	1.6	35.2	1.7
CeO$_2$/Al$_2$O$_3$ based				
3.8Fe/CeO$_2$/Al$_2$O$_3$	50	1.3	65.0	16.0

In the Ce 3d spectra of 3.8Fe/Ce/Al$_2$O$_3$ sample the normal complex form due to shake-down satellites from an O1s to Ce 4f electron transfer observed for CeO$_2$ and 0.86Fe/CeO$_2$ was supplemented by the features marked as v' and u' due to anion defects and Ce^{3+} (Fig. S2) [47]. This means that, besides smaller crystallized CeO$_2$ species, X-ray amorphous CeAlO$_3$ and probably isolated Ce^{3+} species can reasonably form after CeO$_2$ precipitation onto high surface area alumina [48,49], thus stabilizing alumina toward the formation of low-surface-area phases, like proposed in [27].

Therefore, spinel-like surface structures including Al have been formed on the surface of 2.7Co/Al$_2$O$_3$-1200 sample, and probably their mixture with Ni(OH)$_2$ - in 2.7Ni/Al$_2$O$_3$-1200 sample. It is quite reasonable to suppose that above 700^{0}C surface Fe oxyhydroxide formed after Fe supporting onto Al$_2$O$_3$ and all Ni- and Co-containing hydroxylated species convert to corresponding oxides, and thus close types of surface compounds participate in the reaction in both Al$_2$O$_3$-1200, CeO$_2$ and CeO$_2$/Al$_2$O$_3$ based samples.

Table 3 lists the data on the surface concentration of Me in the different Al$_2$O$_3$-1200 and CeO$_2$ based samples. Close values were measured in (2.5-2.7)Me/Al$_2$O$_3$-1200 and 0.91Co(0.86Fe)/CeO$_2$ samples with the same as related per surface unit (6.7*10^{19} at/m^2) content of Me therein that means close MeOx (Co-Al-O) species dispersion (D$_{Me}$) therein. Its relative value can be estimated as follows: D$_{Me}$ = Me$_s$/C$_{Fe}$, where Me$_s$ is the surface atomic concentration of Me in the sample as measured by XPS (Table 3) [%], C$_{Me}$ is total content of Fe in the samples [atoms/m^2]. Noticeably higher content of Ni in the near surface layers of the CeO$_2$ based sample can be explained either by lower degree of Ni penetration into CeO$_2$ resulting in formation of Ni-Ce-O solid solutions (Table 2), or by higher dispersion of NiOx species that agrees well with high content of hydroxylated species.

3.4. ^{18}O SSITKA.

Fig. 5 shows the time dependencies of exchanged oxygen for different samples as related to unit of the surface (N$_O$) calculated using the formulae
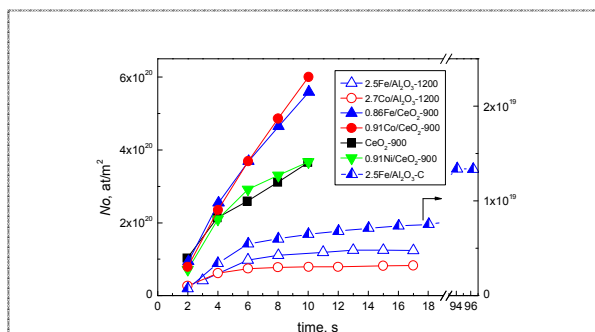

Fig. 5 Time dependence of the quantity of exchanged oxygen (*No*) in ^{18}O SSITKA experiments for different Me/Al$_2$O$_3$ and Me/CeO$_2$ samples.
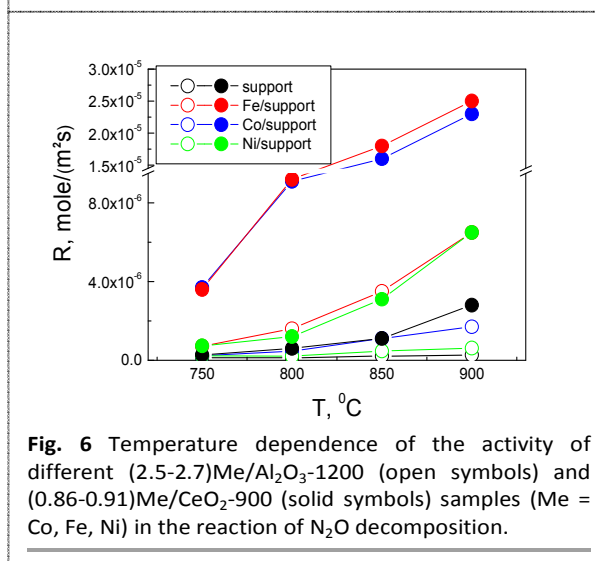

Fig. 6 Temperature dependence of the activity of different (2.5-2.7)Me/Al$_2$O$_3$-1200 (open symbols) and (0.86-0.91)Me/CeO$_2$-900 (solid symbols) samples (Me = Co, Fe, Ni) in the reaction of N$_2$O decomposition.

$$No = N_A \frac{2C_{O_2}U}{S_{BET}\,g}\int_0^t (\alpha_g^{input} - \alpha_g)\,dt$$

where α_g^{input} - isotope fraction in the inlet mixture (0.95), C_{O2} - O$_2$ concentration (mol/mol), U − flow rate of the reaction mixture (mole/s), N_A − Avogadro number. It is seen that for (2.5-2.7)Fe(Co)/Al$_2$O$_3$-1200 samples $N_O(t)$ dependencies (at higher rate of exchange on 2.5Fe/Al$_2$O$_3$-1200, as determined from the slope of N$_o$ curves) reached the plateau after about 15 s after isotope admission corresponding to exchanged 4.9·10^{20} and 3.2·10^{20} O atoms/g for 2.5Fe/Al$_2$O$_3$-1200 and 2.7Co/Al$_2$O$_3$-1200 samples, respectively. With account of the quantity of supported Me (2.7·10^{20} atoms/g), one can suppose that, within the accuracy of measurement, solely the oxygen of Fe$_2$O$_3$ and Co oxidic compounds (Co$_3$O$_4$+Co$_{3-x}$Al$_x$O$_4$) participated in the exchange. The integral quantity of exchanged oxygen in 2.5Fe/Al$_2$O$_3$-C sample (7.9·10^{20} atoms/g) substantially exceeds that in supported Fe oxide. Provided substantially more dispersed FeO$_x$ species have been formed in this sample compared with those in 2.5Fe/Al$_2$O$_3$-1200 one (Table 3), it is more probably support oxygen that can transfer to O$_2$ molecule through developed Fe-alumina interface.

Substantially more profound and faster oxygen exchange took place on CeO$_2$ based samples, obviously involving the bulk of the support starting from the very low time after ^{18}O$_2$ admission. The rate of exchange changed in the following order: 0.91Co/CeO$_2$ ≥ 0.86Fe/CeO$_2$ > 0.91Ni/CeO$_2$ ≈ CeO$_2$ and correlated with values of

red shift of CeO_2 band gap energy (E_g) in turn depending on the content of Me-Ce mixed solution in the sample characterized by increased degree of disorder. Therefore, oxygen transfer from fluorite lattice to surface by extended vacancies arisen after insertion of Me^{n+} ions to fluorite lattice can be responsible for enforced rate of isotope exchange on Me/CeO_2 (Me = Co, Fe) samples compared with pure CeO_2.

3.5. Catalytic activity
3.5.1. N_2O decomposition
Effect of the support nature

Among Al_2O_3-1200 based samples with close as related to surface concentration of supported Me ($6.7*10^{19}$ at/m^2), catalytic activity in N_2O decomposition at T = 750-900 °C can be ordered as follows: $2.5Fe/Al_2O_3$-1200 > $2.7Co/Al_2O_3$-1200 > $2.7Ni/Al_2O_3$-1200 > Al_2O_3-1200 (Fig. 6). $(0.86-0.91)Me/CeO_2$ samples with quite close, both calculated ($6.7*10^{19}$ at/m^2) and real (Table 3), surface concentration of Me as in $(2.5-2.7)Me/Al_2O_3$-1200 samples revealed substantially higher intrinsic activity. In the case of Co and Ni containing samples such rise of the activity could be partly related to formation of principally different state of active component (oxides/hydroxides in CeO_2 case instead of corresponding Co(Ni)-Al-O spinels located on the surface of Al_2O_3). Nevertheless, similar effect observed for Fe based samples characterized by close type of active species on both supports obviously points to the importance of increased oxygen mobility of CeO_2 that in turn was substantially more active than Al_2O_3. Provided the general scheme of N_2O decomposition obeys Langmuir-Hinshelwood mechanism:

1) $N_2O + S \rightarrow N_2O\text{-}S$
2) $N_2O\text{-}S \rightarrow N_2 + O\text{-}S$
3) $2O\text{-}S \leftrightarrow O_2 + 2S$

where S is surface active site, $N_2O\text{-}S$ is adsorbed or chemisorbed N_2O, and O-S is adsorbed or chemisorbed O, the rate of O_2 desorption by step 3) in the case of $(0.86-0.91)Me/CeO_2$ samples increases due to alternative fast supply of oxygen to reduced site S from the subsurface layers (O_{ss}) of CeO_2 characterized by increased bulk oxygen mobility through $Me\text{-}CeO_2$ interface containing a lot of oxygen vacancies to obtain additional O-S site:

4) $O\text{-}S \leftrightarrow O_{ss} + S$

Similar scheme considering two alternative pathways of regeneration of active sites was also proposed for Cu/CeO_2 samples tested in substantially lower temperature range (between 300 and 550 °C) and included recombination step (if two oxidized copper sites are close enough to each other) and the step of Cu^{2+}–O– species reduction by Ce^{3+} [50].

Effect of Fe content and FeOx dispersion

At variation of Fe content in Al_2O_3-1200 based samples from 0.89 to 6.6 wt% (Fe was chosen as the most active among Me) we observed the inverse "activity (as related both to sample surface unit and to one Fe atom) - Fe content" dependence (Fig. 7A). The same Fe_s values for $0.86Fe/Al_2O_3$-1200 and $2.5Fe/Al_2O_3$-1200 samples (Table 3) evidence decrease of FeOx species dispersion (D_{Fe}, Table 3) at higher Fe content. Finally, close rates of N_2O decomposition were measured for bulk Fe_2O_3 and all Fe/Al_2O_3-1200 samples (Fig. S3), although in the former of them Fe_s value should be obviously higher. Therefore, activity of surface Fe sites decreases substantially with enlargement of FeOx species.

At variation of Fe content in CeO_2 based samples from 0.5 to 2.5 wt% (i.e. at close interval of supported Fe to that in the case of Al_2O_3-1200 based samples as related per surface unit and thus close dispersion of FeO_x species) their higher activity due to

increased mobility of oxygen is more prominent at lower quantity of supported Fe. However, activity drop was substantially more prominent, although even higher Fe_s values were measured for the $2.5Fe/CeO_2$ sample than for the $0.86Fe/CeO_2$ one (Table 3). Supposing the rate of oxygen transfer from the bulk to active sites should depend on the length of $MeO_x\text{-}CeO_2$ interface, its decrease at enlargement of FeO_x species (Table 3), revealed as start of oxygen exchange at higher temperature (Fig. S4) should make an additional negative contribution to the activity.

Effect of the support surface area

In accordance with observed effect of FeO_x dispersion onto activity, using of the support characterized by higher specific surface area allows obtaining more dispersed FeOx species at substantially higher total Fe content (Table 3). This opens up additional possibilities for increase of conversion as measured at the same sample loading. Indeed, at close quantity of supported Fe, N_2O conversion increased with S_{BET} value of Al_2O_3 (Fig. 7B).

Unfortunately, for Fe/Al_2O_3-C samples we failed to perform catalytic tests at reasonably low conversion values for correct calculation of the reaction rate values. This fact and substantial negative effect of the quantity of supported Fe on S_{BET} value (Tables 2, 3) complicated analysis of parameters determining the activity. To pass over this problem, we calculated the concentration of exposable FeOx species (Fe_{exp}) per weight unit by following formula: $Fe_{exp} = Fe_s*S_{BET}$, where Fe_s is the surface concentration of Fe as measured by XPS (Table 3), and compared conversion values measured for the same catalyst loading as dependent on both Fe content in the sample and Fe_{exp}. It turned out that N_2O conversion decreased with increase of Fe content from 2.5% to 19.8% (Fig.7B), or FeOx dispersion drop (Table 3), but this order cardinally differed from that for Fe_{exp} ($13.2Fe/Al_2O_3$-C > $6.6Fe/Al_2O_3$-C > $19.8Fe/Al_2O_3$-C > $2.5Fe/Al_2O_3$-C). Therefore, similar to Fe/Al_2O_3-1200 samples, it is the size effect of FeO_x species that seems to be the dominant factor determining descending character of "conversion – Fe content" dependence. Similar reverse dependence was already observed earlier for lower (500-650 °C) temperatures [51]. With account of SSITKA data obtained for $2.5Fe/Al_2O_3$-1200 and $2.5Fe/Al_2O_3$-C samples, higher activity of smaller FeO_x species can be due to growing ability of oxygen supply to reduced active sites S from the alumina regions adjacent to developed MeOx - alumina interface (step 4). Oxygen (3 vol%) and H_2O (3 vol.%) addition into reaction mixture, in accordance with considered above scheme of the mechanism, decreased observed N_2O conversion, but didn't change the order of activity (Fig. S5).
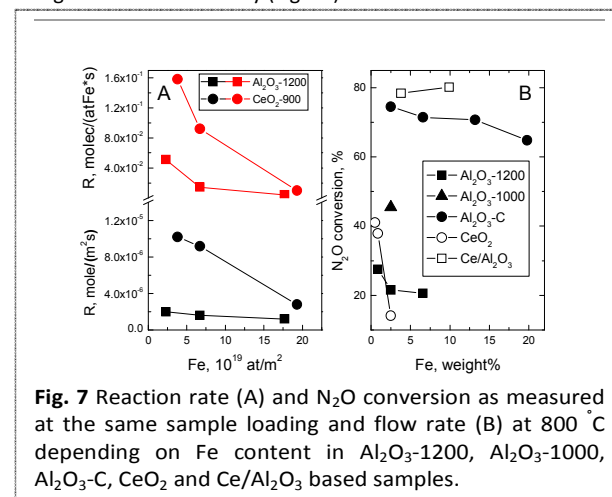

Fig. 7 Reaction rate (A) and N_2O conversion as measured at the same sample loading and flow rate (B) at 800 °C depending on Fe content in Al_2O_3-1200, Al_2O_3-1000, Al_2O_3-C, CeO_2 and Ce/Al_2O_3 based samples.

Effect of CeO_2 dispersion

Using of the effect of high oxygen mobility of CeO_2 for following increase of the efficiency of N_2O decomposition (Fig.7B) is restricted by its low surface area under the reaction conditions [3,20]. Therefore, in addition to traditionally used increase of concentration of active sites by supporting more active component, we tried to disperse CeO_2 by supporting onto high surface area Al_2O_3. Only Fe oxide was used in this case as well to avoid formation low active Ni (Co)-Al spinels. These were 3.8Fe/Ce/Al_2O_3 and 9.9Fe/Ce/Al_2O_3 samples that revealed the highest N_2O conversion (Fig. 7B) due to that part of FeOx therein was anchored to the surface of higher dispersed ceria particles (Table 1, Fig.4c). At the same time, the size effect, at least for the sample 3.8Fe/Ce/Al_2O_3, cannot be completely excluded (compare D_{Fe} values in the Table 3 for the samples 3.8Fe/Ce/Al_2O_3 and 6.6Fe/Al_2O_3-C with close S_{BET}).

3.5.2. NH_3 oxidation
Effect of the support nature

Among (2.5-2.7)Me/Al_2O_3-1200 samples, 2.5Fe/Al_2O_3-1200 one was the most active (Fig. 8A) and characterized by the highest selectivity to NO+NO_2 (86-88%). As the result, the orders for the activity and the efficiency of NO_x formation evaluated as *NO_x yield=Conversion*NO_x selectivity* were close to that for the activity of N_2O decomposition: 2.5Fe/Al_2O_3-1200 >> 2.7Co/Al_2O_3-1200 > 2.7Ni/Al_2O_3-1200 ~ Al_2O_3-1200. In addition, N_2O yield value calculated by similar manner as for *NO_x yield* on 2.5Fe/Al_2O_3-1200 sample in this temperature interval was lower than 2% which is comparable to that for Pt-Rh gauzes [1], while continuous increase of N_2O yield with temperature was noted for all other samples. At lower O_2 concentration in the inlet mixture (2.5%) yield of NO_x decreased to 77-78%, mainly because of lower selectivity. For Co-, Ni- based samples and for pure Al_2O_3-1200 negative changes of conversion and NO_x selectivity were substantially more prominent.

We failed to calculate the rate of ammonia oxidation in all temperature interval due to non-differential reactor operating conditions. Hence, to compare intrinsic activity of samples characterized by different S_{BET} values, we tested catalytic properties of (0.86-0.91)Me/CeO_2 samples at catalyst loading 0.043 g corresponding to the same surface area as for Al_2O_3-1200 based samples. In these conditions already at 750 °C complete NH_3 conversion was measured on all (0.86-0.91)Me/CeO_2 samples, and 96%– for CeO_2 that is obviously due to capability of CeO_2 itself to donate lattice oxygen for ammonia oxidation [16]. Even at the
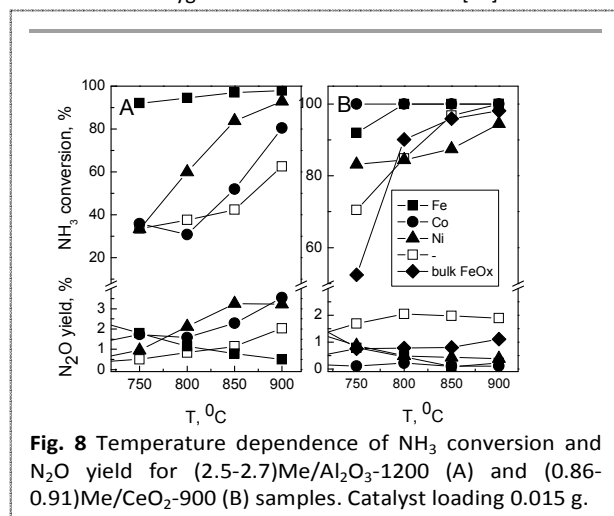
same catalyst loading as for Al_2O_3-1200 based samples (0.015 g), i.e. at about 3 times lower number of Me sites therein (Table 3), higher values of NH_3 conversion were observed for corresponding CeO_2 based samples (Fig.8B). This increase, at least in the case of Fe based samples, is exclusively due to ability of the support to donate oxygen to FeOx, since substantially lower conversion values were measured on CeO_2 and bulk FeO_x characterized by close S_{BET}. N_2O yield values were reasonably lower than on corresponding Al_2O_3-1200 based samples. In addition, at 800^0C the order of NH_3 conversion and NOx yield (not shown for brevity) - 0.91Co/$CeO_2 \geq$ 0.86Fe/CeO_2 > 0.91Ni/$CeO_2 \approx CeO_2$ was exactly the same as for the efficiency towards oxygen exchange therein (Fig.4).

Strong decrease of both NH_3 oxidation [52] and N_2O decomposition [32] over Co oxide at high temperatures was shown to be due to Co_3O_4 reduction to CoO. We didn't observe such deactivation of 0.91Co/CeO_2 sample with temperature both at N_2O decomposition (Fig.6), like in Co_3O_4-CeO_2 mixed oxides with low Co content [11], and at ammonia oxidation (Fig.S7B), although Co_3O_4 reduction under TPD conditions was observed as well (Fig.S6). It obviously can be explained by higher resistance of Co-Ce interface towards reduction due to some oxygen supply from CeO_2 by reaction (4). Nevertheless, at lower temperature 0.91Co/CeO_2 sample with Co state closer to Co_3O_4 was already substantially more active than 0.87Fe/CeO_2 both in N_2O decomposition (Fig.S7A) and NH_3 oxidation (Fig.S7B).

Effect of Fe content and FeOx dispersion

Descending dependence of NH_3 conversion versus Fe content in Al_2O_3-1200 and CeO_2 based samples (0.015 g sample loading for all these experiments) was observed (Fig. 9), similarly to the reaction of N_2O decomposition, and thus can be related to size effect. Again, for Fe/CeO_2 case it was more prominent due to attenuation of oxygen transfer processes through Fe-CeOx interface (Fig.S4). Nevertheless, unlike to reaction of N_2O decomposition, FeOx dispersion is not a predominant factor for NH_3 conversion anymore. So, at Fe content lower than $3*10^{19}$ atoms/m^2 (case of Fe/Al_2O_3-C and Fe/Ce/ Al_2O_3 samples) NH_3 conversion value depended mainly on the quantity of exposable Fe (Fe_{exp}).

At the same time, these were larger FeO_x species that converted NH_3 to NO_x more selectively in all Al_2O_3 based samples (Fig. S8), finally resulting in quite close (77-81%, case of Fe/Al_2O_3-1200 samples) or growing with Fe content (up to 79% for Fe/Al_2O_3-C) NOx yield values (Fig.9). In accordance with findings of Pérez-Ramírez and Kondratenko [16], on bulk Fe_2O_3 the desired reaction follows a Mars–van Krevelen-type scheme involving the
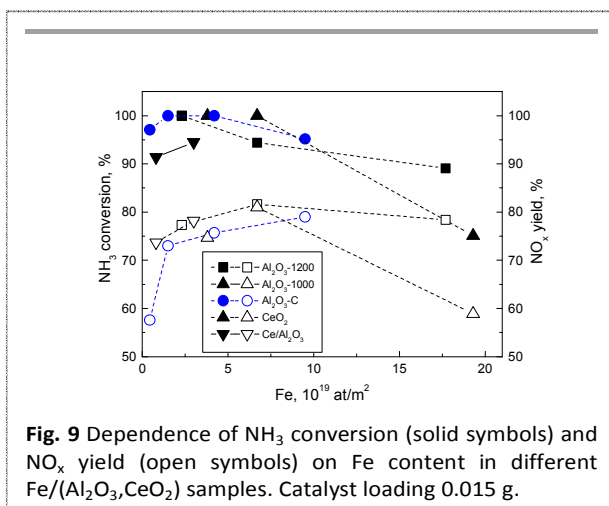

Fig. 8 Temperature dependence of NH_3 conversion and N_2O yield for (2.5-2.7)Me/Al_2O_3-1200 (A) and (0.86-0.91)Me/CeO_2-900 (B) samples. Catalyst loading 0.015 g.

Fig. 9 Dependence of NH_3 conversion (solid symbols) and NO_x yield (open symbols) on Fe content in different Fe/(Al_2O_3,CeO_2) samples. Catalyst loading 0.015 g.

participation of lattice oxygen in the NH$_3$ conversion to NO. The degree of reduction of the oxide surface was shown to determine the product distribution. One can reasonably suppose that for small species FeO$_x$ surface should be in more reduced state because of smaller rate of dissociative activation of O$_2$ molecule on the Fe-Al interface. In addition, growing contribution from low selective NH$_3$ oxidation on Al$_2$O$_3$ should be accounted as well.

We believe as well that more oxidized state of FeOx anchored to CeO$_2$ resulting from more efficient O transfer through Fe-Ce interface determines higher selectivity to NO$_x$ in the 3.8Fe/Ce/Al$_2$O$_3$ and 9.9Fe/Ce/Al$_2$O$_3$ samples compared to Fe/Al$_2$O$_3$-C ones with close dispersion. In addition, substantially smaller values of N$_2$O yield were measured on Fe/Ce/Al$_2$O$_3$ samples, which agrees with their higher activity towards N$_2$O decomposition.

Conclusions

We have shown that replacement of Al$_2$O$_3$ as the support for MeO$_x$ (Me = Fe, Co, Ni) by CeO$_2$ characterized by increased lattice oxygen mobility resulted in substantial increase of the rates of ^{16}O/^{18}O exchange at 800 $^\circ$C in corresponding samples. Oxygen transfer from fluorite lattice to surface by extended oxygen vacancies arose after insertion of Me^{n+} ions to fluorite lattice was shown to be responsible for enforced rate of isotope exchange.

Formation of low active spinel-like Me-Al-O structures restricted application of Co and Ni oxides in any Al$_2$O$_3$ containing catalysts. For CeO$_2$- and Al$_2$O$_3$-based samples with supported FeO$_x$ an obvious size effect was observed in both reactions. So, highly dispersed FeO$_x$ were substantially more active due to change of contribution of oxygen supply from the support (both ceria and, probably, alumina) to reduced surface sites through Fe-CeO$_x$ interface thus increasing the rate of O$_2$ desorption. However, smaller species less selectively oxidized NH$_3$ to NO$_x$.

Using of high surface area Al$_2$O$_3$-C the samples with high content of dispersed FeO$_x$ in the weight unit were synthesized to increase observable N$_2$O conversion. To increase surface area of CeO$_2$ and thus efficiently use the promoting effect of oxygen mobility, the last was dispersed onto alumina by precipitation. Fe/Ce/Al$_2$O$_3$ samples with optimal content of Fe revealed superior activity in N$_2$O decomposition and NH$_3$ oxidation to NOx compared with Fe/Al$_2$O$_3$ with close S$_{BET}$ and dispersion of FeO$_x$ species value.

Acknowledgements

Notes and references

1 J. Pérez-Ramírez, F. Kapteijn, K. Schöffel, J.A. Moulijn, *Appl. Catal. B,* 2003, **44**,) 117.

2 P. Granger, P. Esteves, S. Kieger, L. Navascues, G. Leclercq, *Appl. Catal. B*, 2006, **62**, 236.

3 P. Esteves, Y. Wu, C. Dujardin, M.K. Dongare, P. Granger, *Catal. Today*, 2011, **176**, 453.

4 D.V. Ivanov, E.M. Sadovskaya, L.G. Pinaeva, L.A. Isupova, *J. Catal.*, 2009, **267**, 5.

5 Y. Wu, X. Ni, A. Beaurain, C. Dujardin, P. Granger, *Appl. Catal. B*, 2012 **125**, 149.

6 D.V. Ivanov, L.G. Pinaeva, L.A. Isupova, E.M. Sadovskaya, I.P. Prosvirin, E.Yu. Gerasimov, I.S. Yakovleva, *Appl. Catal. A*, 2013 **457**, 42.

7 J. Pérez-Ramírez, M. Santiago, *Chem. Commun.,* 2007, 619.

8 G. Giecko, T. Borowiecki, W. Gac, J. Kruk, *Catal. Today*, 2008, **137,** 403.

9 J. Kruk, K. Stołecki, K. Michalska, M. Konkol, P. Kowalik, *Catal. Today*, 2012, **191,** 125.

10 E. Wilczkowska, K. Krawczyk, J. Petryk, J. W. Sobczak, Z. Kaszkur, *Appl. Catal. A*, 2010, **389**, 165.

11 E. Iwanek, K. Krawczyk, J. Petryk, J.W. Sobczak, Z. Kaszkur, *Appl. Catal. B*, 2011, **106**, 416.

12 M. Konsolakis, *ACS Catal.*, 2015, **5**, 6397.

13 V.A. Sadykov, L.A. Isupova, I.A. Zolotarskii, L.N.Bobrova, A.S. Noskov, V.N. Parmon, E.A. Brushtein, T.V. Telyatnikova, V.I. Chernyshev, V.V. Lunin, *Appl. Catal. A*, 2000, **204**, 59.

14 L. Pinaeva, E. Sutormina, L. Isupova, N. Kulikovskaya, A. Marchuk, *RU patent 2 430 782 C1*, 2010.

15 L. Pinaeva, L. Isupova, I. Prosvirin, E. Sadovskaya, I. Danilova, D. Ivanov, E. Gerasimov, *Catal. Lett.,* 2013, **143**, 1294.

16 J. Pérez-Ramírez, E. Kondratenko, *J. Catal.,* 2007, **250**, 240.

17 M. Zabilskiy, B.Eravec, P.Djinović, A. Pintar, *Chem. Eng. J.*, 2014, **254**, 153.

18 M. Konsolakis, S. A. C. Carabineiro, E. Papista, G. E. Marnellos, P. B. Tavares, J. Agostinho Moreira, Y. Romaguera-Barcelay, J. L. Figueiredo, *Catal. Sci. Technol.*, 2015, **5**, 3714

19 L. Isupova, Yu. Tanashev, I. Kharina, E. Moroz, G. Litvak, N. Boldyreva, E. Paukshtis, E. Burgina, A. Budneva, A. Shmakov, N. Rudina, V. Kruglyakov, V. Parmon, *Chem. Eng. J.*, 2005, **107**, 163.

20 I. Danilova, E. Slavinskaya, V. Zaikovskii, A. Ivanova, A. Boronin, R. Gulyaev, Yu. Amosov, *Kinet. Catal.,* 2010, **51**, 143.

21 J. Tauc, R. Grigorovici, A. Vancu, *Phys. Stat. Sol.*, 1966, **B15**, 627.

22 V. Malakhov, N. Boldyreva, A. Vlasov, L. Dovlitova, *J. Analyt. Chem.,* 2011, **66**, 458.

23 L.G. Pinaeva, E.M. Sadovskaya, A.P. Suknev, V.B. Goncharov, B.S. Bal'zhinimaev, in *Mass Spectrometry Handbook,* (Ed.: M. S. Lee), Wiley, Hoboken, **2012**, pp. 1229-1256.

24 S. Kurajica, J. Popović, E. Tkalčec, B. Gržeta, V. Mandić, *Mater. Chem. Phys.*, 2012, **135**, 587.

25 O. Kirichenko, V. Ushakov, E. Moroz, M. Vorob'eva, *Kinet. Catal.,* 1993, **34**, 739.

26 Z. Zhang, D. Han, S. Wei, Y. Zhang, *J. Catal.*, 2010, **276**, 16.

27 A. Gupta, A. Kumar, U.V. Waghmare, M.S. Hegde, *Chem. Mater.*, 2009, **21**, 4880.

28 A. Piras, S. Colussi, A. Trovarelli, V. Sergo, J. Llorca, R. Psaro, L. Sordelli, *J. Phys. Chem. B*, 2005, **109**, 11110.

29 A. Bensalem, J.C. Muller, F. Bozon-Verduraz, *J. Chem. Soc. Faraday Trans.*, 1992, **88**, 153.

30 R. Zhang, J.T. Miller, C.D. Baertsch, *J. Catal.*, 2012, **294**, 69.

31 R.C. Olegário, E.C.F. Souza, J.F.M. Borges, J.B.M. Cunha, A.V.C. Andrade, S.R.M. Antunes, A.C. Antunes, *Dyes Pigments,* 2013, **97**, 113.

32 C. He, M. Paulus, W. Chu, J. Find, J.A. Nickl, K. Kohler, *Catal. Today,* 2008, **131**, 305.

33 I.G. Casella, M.R. Guascito, *J. Electroanal. Chem.,* 1999, **476**, 54.

34 H. Xiong, Y. Zhang, K. Liew, J. Li, *J. Molec. Catal. A,* 2005, **231**, 145.

35 M.H. Kim, K.-H. Choo, *Catal. Comm.*, 2007, **8**, 462.

36 J. Yang, H. Liu, W.N. Martens, R.L. Frost, *J. Phys. Chem.,* 2010, **C114**, 111.

37 X. Duan, M. Pan, F. Yu, D. Yuan, *J. Alloys Comp.,* 2011, **509**, 1079.

38　N. Srisawad, W. Chaitree, O. Mekasuwandumrong, P. Praserthdam, J. Panpranot, *J. Nanomaterials*, 2012, **2012**, 1.

39　D. Barreca, C. Massignam, *Chem. Mater.,* 2001, **13**, 588.

40　S.C. Petitto, E.M. Marsh, G.A. Carson, M.A. Langell, *J. Mol. Catal. A*, 2008, **281**, 49.

41　D. Nikolova, R. Edreva-Kardjieva, G. Gouliev, T. Grozeva, P. Tzvetkov, *Appl. Catal. A*, 2006, **297**, 135.

42　P. Dufresne, E. Grimblot, J.P. Bonnelle, *J. Phys. Chem.*, 1981, **85**, 2344.

43　E. Laurent, B. Delmon, *J. Catal.,* 1994, **146**, 281.

44　C. Jiménez-González, Z. Boukha, B. de Rivas, J.J. Delgado, M.A. Cauqui, J.R.González-Velasco, J.I. Gutiérrez-Ortiz, R. López-Fonseca, *Appl. Catal. A*, 2013, **466**, 9.

45　P. Prieto, V. Nistor, K. Nouneh, M. Oyama, M. Abd-Leftil, R. Diaz, *Appl. Surf. Sci.*, 2012, **258**, 8807.

46　S.Suzuki, K.Yanagihara, K.Hirokawa, *Surf. Interface Anal.*, 2000, **30**, 372.

47　L. Chen, P. Fleming, V. Morris, J.D. Holmes, M.A. Morris, *J. Phys. Chem. C*, 2010, **114**, 12909.

48　J. Z. Shyu , W. H. Weber , H. S. Gandhi, *J. Phys. Chem.,* 1988, **92**, 4964.

49　C. Ge, L. Liu, Z. Liu, X. Yao, Y. Cao, C. Tang, F. Gao, L. Dong, *Catal. Commun.,* 2014, **51**, 95.

50　M. Zabilskiy, P. Djinović, E. Tchernychova, O. Tkachenko, L. Kustov, A. Pintar, *ACS Catal.*, 2015, **5**, 5357.

51　P. Pomonis, D. Vattis, A. Lycourghiotis, C. Kordulis, *J. Chem. Soc. Faraday Trans. I*, 1985, **81**, 2043. 52 M. C. Goromonzi, S, K. Raman, B. D. Padalia, A. Manohar, P. N. Koul, *React. Kinet. Catal. Lett.,* 1980, **15**, 131.